Chapter 3:
New Methodology for Estimating CO_2

This chapter depicts the part of the present studies conducted with the spatial distribution of the atmospheric carbon dioxide (CO_2) abundance and the new methodologies developed in this connection. A technique for averaging the CO_2 absorption depths, referred to as *a*-DOAS is suggested in terms of linear sum of band radiance. A methodology is put forward for water vapour correction on the CO_2 absorption depth by comparison with the spectral radiance of Mars' atmosphere. All proposed techniques are validated with airborne hyperspectral images.

3.1. Materials and Method

This work consists of ground-based spectroradiometric measurements and analysis of the hyperspectral images procured by Airborne Visible/Infrared Spectrometer Next Generation (AVIRIS-NG) flown for the first time over the sky of India. The mission was conducted jointly by Space Applications Centre, Indian Space Research organization (SAC-ISRO), Govt. of India and Jet Propulsion Laboratory, National Aeronautics and Space Administration (JPL, NASA) during February-March, 2016.

3.1.1. Ground Measurements

The regions of interest were part of two adjacent cities, namely Howrah (around 22° 33′ 30″ N, 88° 17′ 30″ E) and Kolkata (around 22° 32′ 30″ N, 88° 19′ 30″ E) situated on either side of Hooghly River. Field work was conducted in these regions for the following three types of measurements.

(A) Solar Irradiance Spectra: The solar irradiance values for the wavelength range of 0.35 –2.50 μm were measured at different urban sites of varying population density and vehicle congestion in open air cloud-free solar illumination with Analytical Spectral Devices (ASD) spectroradiometer. The spectral sampling interval was of 0.0014 μm for 0.350 – 1.0 μm and of 0.002 μm for 1.000 – 2.500 μm. The instrument was held vertically sky-facing and the following two types of spectral measurements were taken.

- Narrow angle (1° FOV) fore optic accessory fitted on the 25° FOV fiber
- Wide angle (180° FOV) remote cosine receptor fitted on the 25° FOV fiber

The narrow angle spectral data denoted the radiance spectra and the wide angle (integrated over 180°) data represented the irradiance spectra. The objective was to distinguish between the effects of the directly incident solar radiation and that diffused over the hemisphere. The ground truth data acquisition processes were carried out corresponding to the sensor flight in order to understand the appropriate effects of the atmospheric scattering and surface reflection characteristics on the imaging.

(B) Solar Reflectance Spectra: The reflectance spectra were measured with the same ASD spectroradiometer with the same spectral range and resolution for different surfaces, such as grass, soil and man-made objects like concrete and asphalt. A spectralon white reference panel was used for estimating the reflectance values.

(C) Local CO_2 Concentration: The local atmospheric CO_2 concentrations (ppm) at the ground level were measured simultaneously with handheld carbon dioxide meter Model GCH-2018. The solar illumination at the measuring spot was recorded with Metravi light intensity meter. It provided ancillary data for correlating the ground-level solar illumination with the corresponding radiance recording that might be useful to developing some model in future for the possible vertical profiles of CO_2 concentration. The recording of solar illumination at the measuring spot with the light intensity meter kept a provision for retrieving the spectral power distribution with the assumption of 683 lux equivalent to 1 Wm^{-2} at 555 nm.

3.1.2. AVIRIS-NG Image Analysis

The AVIRIS-NG hyperspectral images in the above-mentioned flight mission were procured over different sites throughout India. Among those, the images for the regions corresponding to the above-mentioned ground measurements were selected. The

wavelength range covered by the images is 0.3764 – 2.5001 μm at 0.005 μm interval. The spatial resolution for the flight varied from 4 to 8 m with flight altitude varying from 4 to 8 km. Also, some Hyperion images downloaded from USGS website (detailed in Chapter 5) were used for comparison of detection of CO_2 absorptions on the solar radiance spectra. The hyperspectral radiance data were derived from these images using ENVI 5.3 image processing software.

3.1.3. Methodology for a-DOAS

Two consecutive CO_2 absorption bands, henceforth denoted by CO_2-1 and CO_2-2, respectively, were noted on both the hyperspectral image-derived and the ground-measured radiance spectra at around 2 μm. The CO_2 concentrations were retrieved individually from both the absorption depths obtained from the AVIRIS-NG images by developing the following algorithm. It is actually a modified version of the standard differential optical absorption spectroscopy (DOAS) where an averaging is done for the radiance values of the AVIRIS-NG wavebands within and around the CO_2 absorption bands. Hence the method is named as *a*-DOAS technique.

The AVIRIS-NG channels comprise narrow, contiguous wavebands, each of about 5 nm and more than one such channels are accommodated to the CO_2 absorption bands. In order to represent their collective effect and to level out the effect of surface reflectance over these bands, the absorption depths are defined in terms of weighted average of the radiance over several bands at the absorbing and the non-absorbing wavelengths. The reference radiance $L_0(\lambda)$ at the wavelength (λ_a) of maximum absorption is defined as

$$L_0 = w_s L_s + w_l L_l \tag{3.1}$$

In Eq. (3.1), L_s and L_l represent the mean radiance values at non-absorbing mean wavelengths outside the absorption band; shorter (λ_s) and longer (λ_l) wavelengths, respectively, with reference to the mean wavelength of maximum absorption (λ_a). The corresponding weighting functions are given by

$$w_s = (\lambda_l - \lambda_a)/(\lambda_l - \lambda_s) \tag{3.1a}$$

and

$$w_l = (\lambda_a - \lambda_s)/(\lambda_l - \lambda_s) \tag{3.1b}$$

If L_a be the actual mean radiance at the wavelength (λ_a) of maximum absorption, the atmospheric path be of length z and c be the mean CO_2 concentration (molecules/cm^3) over the whole atmospheric column of length z. The magnitude of CO_2 absorption of radiation throughout the atmospheric column can be estimated as

$$\ln[L_0(\lambda)/L_a(\lambda)] = \sigma(\lambda)cz \tag{3.2}$$

The parameter $\sigma(\lambda)$ in Eq. (3.2) represents the narrowband component of absorption cross-section (cm^2/molecule) rapidly varying with wavelength around the absorption band. The reference radiance $L_0(\lambda)$ takes care of Rayleigh and aerosol scattering, if any, in the above modified formulation for differential absorption of spectral radiance. It is worth mentioning that the above equations is generalized and can be implemented to any gaseous absorption. In the case of AVIRIS-NG, the bands involved in the calculation of radiance L_s, L_l and L_a and the wavelengths λ_s, λ_l and λ_a (hence the determination of L_0) are specified in Table 3.1.

Table 3. 1. AVIRIS-NG band numbers for calculating mean radiance at absorbing (λ_a) and non-absorbing (λ_s and λ_l) wavelengths of the CO_2-1 and CO_2-2 absorption bands

Mean Radiance	CO_2-1		CO_2-2	
	Band Numbers involved	Mean wavelength (μm)	Band Numbers involved	Mean wavelength (μm)
L_s	322, 323 and 324	λ_s = 1.989	332, 333 and 334	λ_s = 2.039
L_a	326, 327 and 328	λ_a = 2.009	336, 337, 338 and 339	λ_a = 2.059
L_l	332, 33 and 334	λ_l = 2.039	341, 342, 343, 344 and 345	λ_l = 2.089

If the above equations were applied directly to the AVIRIS-NG wavebands, the calculated absorption depths might be screened by the widely varying surface reflected

radiance from pixel to pixel. Therefore, the radiance value (L_i) for each image pixel of each *i*-th band was normalized in the following way. Five spectral subsets, each containing the two CO2 absorption bands and several surrounding bands were taken out from different portions of the hyperspectral image cube. For each of these subset images, 100 spectra were collected for random pixels of different surface features. Collecting the spectra, band 315 (1.949 μm) and band 346 (2.104 μm) were recognized as the bands corresponding to the minimum and the maximum radiance, respectively, for this spectral range. The distinctness of the images in these bands were ensured. The radiance of each pixel of each concerned band (Table I) was normalized in terms of these two bands. The normalized radiance (Li(norm)) for the radiance value (Li) of each image pixel of each i-th band is expressed as

$$L_{i(\text{norm})} = (L_i - L_{\min})/(L_{\max} - L_{\min}) \tag{3.3}$$

The symbols $L_{\min}$ and $L_{\max}$ represent the radiance value at band-315 and band-349, respectively.

It has been reported (Raychaudhuri et al. 2019) that the surface reflectance does not change remarkably over the wavelength range of CO_2 absorptions around 2 μm. So, the averaging of the normalized bands is expected to minimize the influence of wavelength variation of surface reflectance on the estimation of CO_2 absorption depths.

The radiance ratio (L_0/L_a) was calculated [Eq. (3.1)] for both the normalized and the original bands and a multiplicative factor was thus obtained for the actual band radiance value, which was used in determining the actual CO_2 concentration (c) from the original image with Eq. (2). The AVIRIS-NG images have high spatial resolution that makes the pixel-to-pixel variation of radiance, the key factor to determine the CO_2 concentration too fine in spatial resolution. A spatial averaging was done by convolution and low pass filtering with kernel size of 11×11 pixels.

Several sets of ground based non-absorbed (L_0) and absorbed (L_a) radiance values for CO_2 were prepared from the concurrent ground-based spectral measurements mentioned above. Form both narrow and wide angle measurements of the incident solar

radiation, the effective values of CO_2 absorption cross-section were estimated and utilized, as mentioned in the next section.

3.1.4. Correction for Sensor Altitude

A space-borne CO_2 sensor, such as OCO-2 remains well above the atmospheric altitude thereby ensuring the assessment of the total CO_2 column. The present case is, however, that of an airborne sensor whose flight altitude varied from 3 to 5 km. Use of those values directly in Eq. (3.2) might not be appropriate. That would result in overestimate or underestimate of the CO_2 concentration because the absorption depth is not supposed to undergo linear change with altitude. In order to get rid of such discrepancy, the following technique was implemented.

CO_2 absorptions on solar radiance spectra at various observation heights were simulated using the MODTRAN6 (Spectral Sciences Inc.) code for a tropical environment with a CO_2 concentration of 400 ppm over a wide range of observation heights from ground level up to 30 km. Figure 3.1 depicts the simulated change in absorption depth $\tau(z)$ as a function of altitude (z). To understand the variation of the simulated absorption depth along altitude, observations were conducted for I the incoming area where the incident radiation is detected by constantly reducing the observer height from 30 to 0 km and (ii) the reflected region where the observer records the ground reflected radiation by elevating from 0 to 30 km. The ground surface functions as a transition point in the course of the observer's above motions, creating a change in direction for both movement and radiation detection. To maintain a smooth transition up to the reflected area, the observation height at the incoming region is regarded negative, such that the radiation path length grows constantly. After around 15 kilometers in both zones, the ratio starts to saturate. The change with height is sigmoidal rather than linear, showing that CO_2 is not uniformly distributed in the atmosphere and is more densely packed near the ground surface. The following Boltzmann sigmoidal equation was used to fit the sigmoid-like fluctuation of absorption depth [$\tau(z)$] with altitude (z).

$$\tau(z) = \frac{\tau_i - \tau_r}{1+\exp\frac{(z-z_0)}{dz}} + \tau_r \quad (3.4)$$

where τ_i and τ_r are the incoming and reflected absorption depths at 30 km altitude, respectively. The altitude z_0 corresponds to the absorption depth $(\tau_i + \tau_r)/2$, and dz is the slope of the curve at z_0 such that $(z_0) = (\tau_r - \tau_i)/ (4dz)$.

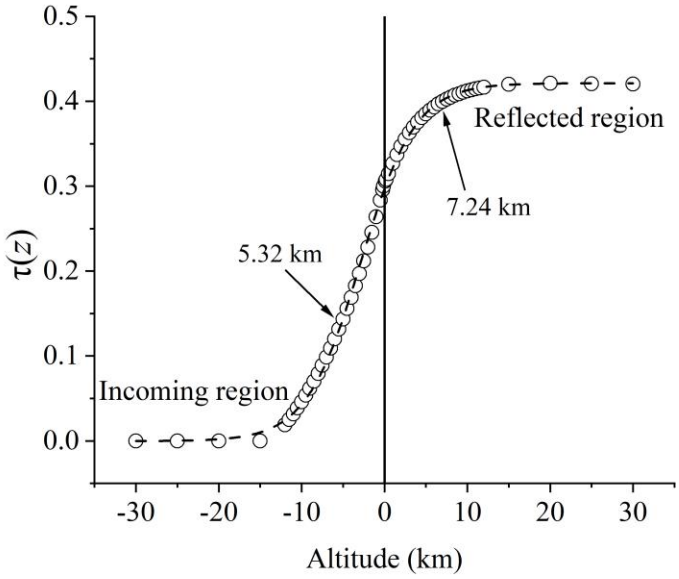

Figure 3. 1. Variation of MODTRAN6 simulated absorption depth τ(z) (hollow circles) fitted with Eq. (3.4) (dashed line). The transition point of the ground surface is indicated by the solid line.

Fitting the distribution of CO_2 concentration throughout the altitude with Eq. (3.4), it is understood that for unit change of absorption depth, the change in atmospheric height is larger at higher altitudes and smaller near ground level, implying a more rapid change of absorption depth at lower altitudes and the effective atmospheric absorption depth being inclined to lower altitudes. The effective optical is defined as the standard deviation and the central peak in the distribution of the rate of change in absorption depth $[\tau(z)/z]$ over altitude. The central peak is relocated to the ground level, which is predicted to have the highest CO_2 concentration. As a result, the effective optical path for incident solar radiation (associated with field spectroscopy) is defined as the standard deviation at the incoming region (6.28 km) plus the shift of the central peak (-0.96 km in this instance).

The atmospheric pathlength for reflected radiation (applicable to AVIRIS-NG) was calculated as the effective optical path length plus the sensor height, taking into account absorption for both incoming and reflected radiation. As shown in Figure 3.1, the aforementioned values in this scenario become 5.32 km for incoming radiation and 7.24 km for reflected radiation. By plugging 5.32 km as z into Eq. (3.2) along with the L_0 and L_a values measured from field spectroscopy. The average CO_2 concentration derived from OCO-2 database for the same date of AVIRIS-NG flight and for the region covering that of the field work was taken as the reference value. Thus, a mean value of the effective absorption cross-section (σ) was determined from Eq. (3.2). Using that value of σ, the CO_2 concentration was calculated from the L_0 and L_a values derived from AVIRIS-NG. Table 3.1 and Eq. (3.1) are referred to. For the reflected radiation, the atmospheric path length was predicted as the effective optical path of the incoming region (5.32 km) plus the sensor altitude (which varies depending on location), accounting absorption for both the incoming and reflected radiation.

Sections 3.1.3 and 3.1.4 together put up the *a*-DOAS technique developed in this work. The method has the following advantages.

- The entire process is based on image-derived and ground-measured data. No other calibration data, such as extraterrestrial radiance is required.
- The normalization of radiance has the merit of minimizing the wide variation of surface reflected radiance from pixel to pixel.
- The band averaging reduces the effect of wavelength dependence of surface reflectance.

3.2. Ground-Measured and Image-Derived Spectra

Before going to any quantitative analysis, the general findings from the ground-measured and image-derived high-resolution spectra are introduced. The reasonableness of the spectroscopic assessment method outlined in the previous section is validated with the outcomes of the spectral standardizations mentioned here.

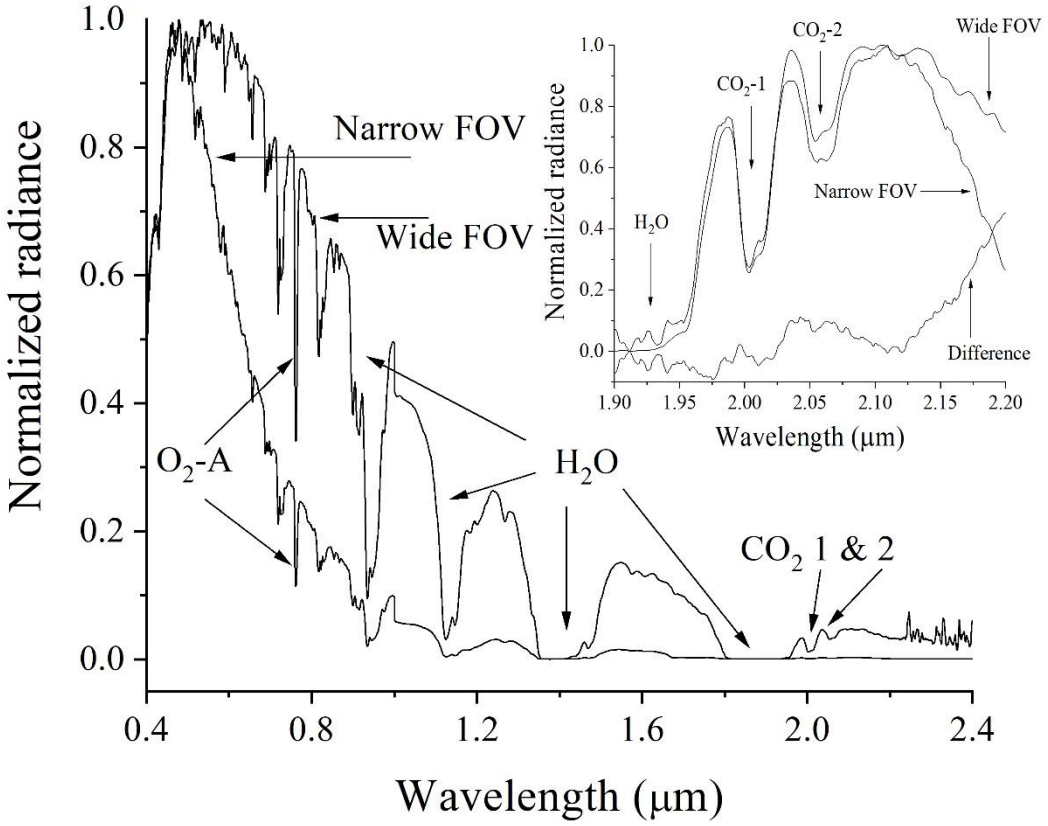

Figure 3. 2. Sample solar radiance spectra for a typical urban site measured with ASD spectroradiometer for narrow and wide-angle fields-of view. The inset shows an enlarged view around CO_2 absorption bands (1 & 2). The water vapor (H_2O) and oxygen (O_2-A) absorption bands are indicated on the spectra.

3.2.1. General Hyperspectral Features

Figure 3.2 shows a sample of the directly incident solar radiance spectra measured with ASD spectroradiometer at a typical urban site for both narrow angle field-of-view (FOV) recording the direct solar radiation and wide angle FOV including the diffused radiation arising from atmospheric scattering. The actual radiance values in these two cases were, obviously, quite different. In order to bring the spectra within the same scale, as shown in Figure 3.2, each spectral curve is normalized with respect to the corresponding maximum radiance value over the total wavelength range. Figure 3.3 shows a sample of AVIRIS-NG image-derived hyperspectral radiance for densely populated urban regions varying over the same wavelength range as that of Figure 3.2.

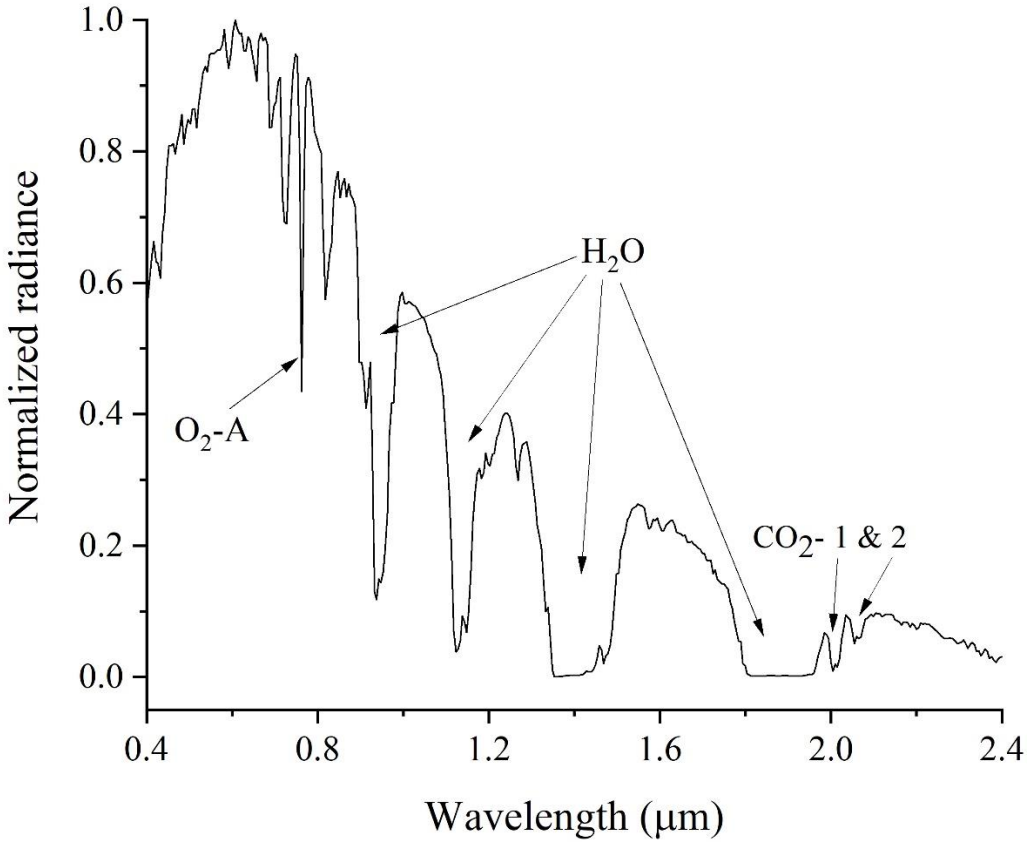

Figure 3. 3. A sample of AVIRIS-NG image-derived hyperspectral radiance variation over 0.4 to 2.4 μm for densely populated urban region.

Both figures 3.2 and 3.3 yield similar features of atmospheric absorption of solar radiation. The features of Figure 3.2 are elaborated in detail. The major atmospheric absorptions, such as the oxygen absorption (O_2-A) around 0.761 μm and the several water vapor absorption bands (H_2O) are located on the spectral curves. As mentioned earlier, two consecutive CO_2 absorption depths, designated as CO_2-1 and CO_2-2 are noted on the spectra at around 2 μm. These two absorption depths are used in this work for estimating CO_2 concentration. Therefore, these are highlighted in the inset that magnifies a short segment of the spectra over the wavelength range of 1.9 to 2.2 μm containing the CO_2-1 and CO_2-2 absorption bands. The bands are visible on the wide angle spectrum but not on the narrow angle spectrum only because of the two different spectral shapes. The enlarged view of the inset of Figure 3.2 ensures that the CO_2 bands are present in both cases. Here

the original radiance values of each spectrum are normalized with respect to the maximum radiance value within this short range only.

3.2.2. Spectral Standardizations

The two consecutive CO_2 absorption depths, referred to as CO_2-1 and CO_2-2 around 2 µm were noted on all the spectral irradiance curves obtained from three independent spectral sources, namely ASD spectroradiometer (ground-based), AVIRIS-NG (airborne) and Hyperion (space-borne). Table 3.2 presents a comparison of the absorption wavelengths corresponding to CO_2-1 and CO_2-2 obtained from these three.

Table 3. 2. Comparison of the absorption maxima for atmospheric carbon dioxide (CO_2-1 and CO_2-2) obtained from ground-, air- and space-based spectra.

Date Source	Sensor altitude	Wavelength (µm) for absorption maximum		Deviation (%) from ground-based result
		CO_2-1	CO_2-2	
ASD spectroradiometer	0 – 23 m	2.003 – 2.006	2.053 – 2.057	0
AVIRIS-NG	6 – 7 km	2.004	2.054	0.3 – 0.8
Hyperion monsoon season	705 km	2.002	2.052	0.6 – 0.7
Hyperion winter season	705 km	2.002	2.052	0.6 – 0.7

It is important to recall that the actual molecular vibration phenomenon of radiation absorption by an atmospheric gas is of sub-nanometer resolution whereas all these sensors have the resolution of several nanometers. So it is necessary to standardize the results taking into account the effects of sensor altitude and spectral resolution on the detection of absorption. The ground-based spectroradiometer is free from the effect of surface reflectance. Considering this measurement of radiation absorption through the atmospheric column as the standard one, the AVIRIS-NG and Hyperion data are

compared with it. It is found that these are in good agreement irrespective of the present variation of sensor position and spectral resolution thereby ensuring consistent result from ground-based and airborne remote measurements.

It is observed from both Figure 3.2 and Figure 3.3 that one of the water vapour (H_2O) absorption bands existing adjacent to CO_2-1 band encroaches a portion of the actual CO_2 absorption in this band. A correction technique for the same is proposed later in this chapter. The other CO_2 absorption band, namely CO_2-2 band is more or less free from water vapor absorption. So this band is chosen for the initial assessments.

Table 3. 3. Comparison of non-absorbed and absorbed radiance ratio for narrow and wide angle ground measurements at four independent urban sites calculated for CO_2-2 band.

Site No.	Non-absorbed (L_0) to absorbed (L) radiance ratio	
	Narrow angle FOV	Wide angle FOV
1	1.466	1.485
2	1.412	1.413
3	1.485	1.452
4	1.445	1.432

The non-absorbed (L_0) to absorbed (L) radiance ratio for narrow and wide angle FOVs obtained from field spectroscopy were determined for four independent urban sites using the CO_2-2 band. The results, displayed in Table 3.3 lead to a very useful inference. The values of the ratio for the narrow angle (direct incidence) and the wide angle (atmospheric scattering) radiance are found to be almost the same, which indicates that the effect of atmospheric scattering is the same at the wavelengths inside and outside the absorption band and does not hamper the absorption depth assessment by *a*-DOAS method put forward in section 3.1.3. Also, as noted from the expanded view of the inset in Figure 3.2, the difference of the measured radiance at narrow and wide angle FOVs shows a very little change with wavelength over the range of the two CO_2 absorption bands and increases beyond that range. This is also a supporting feature for *a*-DOAS that makes use of weighted average of wavebands around the CO_2 absorptions.

3.3. Results on CO_2 Concentration

Figure 3.4 presents several examples of reflectance of different surface features derived from field spectroscopy (Section 3.1.1). The extended view for the wavelength span around the CO_2 absorption bands is given in the inset. It is noted that the reflectance values for different features differ widely from one another but the reflectance value for a certain feature does not change much with wavelength over this range. Utilizing this fact, the reflectance values of different pixels in AVIRIS-NG images were normalized using Eq. (3.3). Figure 3.5 demonstrates the reflected radiance conditions before and after the normalization with several sample spectra. The normalization brings the CO_2 absorption depth for different surface features up to the same scale.

Figure 3.6(a) shows a sample AVIRIS-NG image segment containing distinct features like waterbody (W), vegetated (V) and non-vegetated urban (U) regions that are expected to contain different CO_2 concentrations. The *a*-DOAS algorithm of section 3.1.3 when applied to these images, the spatial distribution of CO_2 estimated from CO_2-2 band is derived as that presented in Figure 3.6(b). Comparing the two figures, it becomes apparent that the vegetated regions possess lower concentration of CO_2. The overall concentration is much larger than the global average (around 415 ppm) but this is reasonable because the entire area is densely populated urban region.

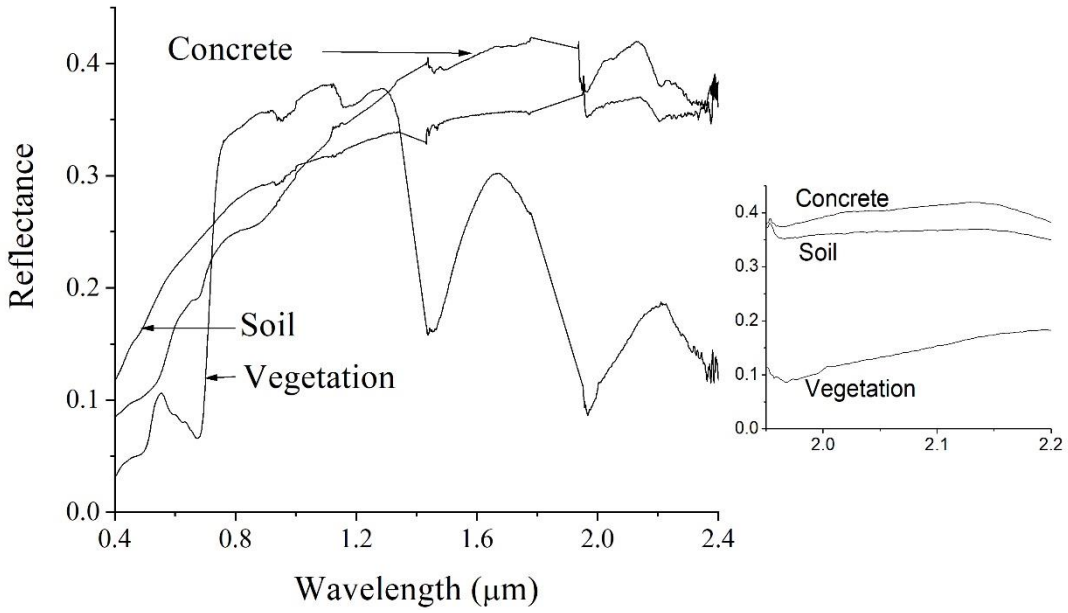

Figure 3. 4. Samples of field measured surface reflectance spectral curves for three different surface features, namely grass, soil and concrete; the inset showing an expanded view for the CO_2 absorption bands.

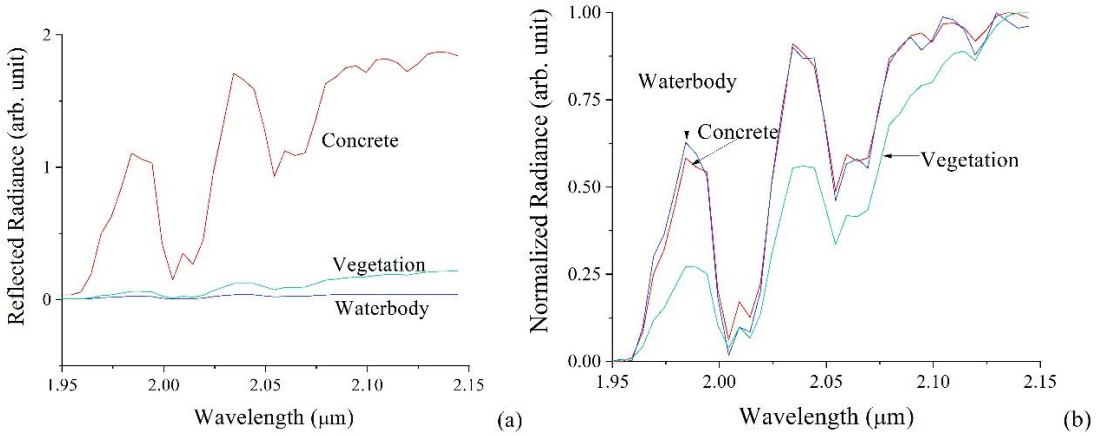

Figure 3. 5. Wavelength dependence of the reflected radiance over the CO_2 absorption bands for different surface features, namely Waterbody, Vegetation and Concrete derived from AVIRIS-NG image: (a) Original condition in DN value and (b) After normalizing with Eq. (3.3).

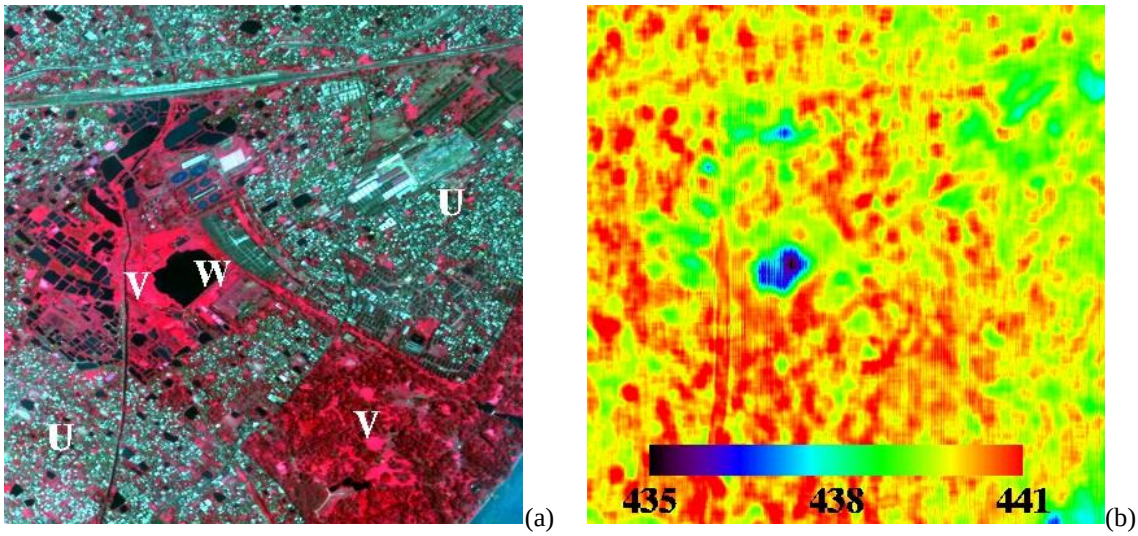

(a) (b)

Figure 3. 6. (a) A segment of AVIRIS-NG image containing distinct waterbody (W), vegetated region (V) and non-vegetated urban zone (U) and (b) the corresponding spatial distribution of CO_2 concentration (ppm) estimated from CO_2-2 band.

3.4. Water Vapour (H_2O) Correction

If one intends to estimate the CO_2 concentration in the same way as above utilizing the other CO_2 absorption band (CO_2-1), the effect of the adjacent water vapour (H_2O) absorption band should be taken into account. As illustrated in section 3.2.2, the atmospheric H_2O gives rise to several absorption bands throughout the infrared wavelengths of solar radiation and one of those bands partly overlaps that of CO_2 absorption band around 2 μm (figures 3.1 and 3.2) thereby distorting both the shape and the depth of the CO_2 absorption band. It is of utmost importance to recover the average CO_2 absorption profile from the spectral radiance curve, particularly for the medium resolution spectrometers like those of the present work. Therein lies the importance of H_2O correction in connection with CO_2 assessment. The present work has developed two different techniques for this purpose, illustrated in this section and the next one, respectively.

In order to present a visual interpretation for the H_2O absorption encroaching the CO_2 absorption, model radiance spectra for tropical urban atmosphere under different conditions of atmospheric water vapor were simulated with MODTRAN6 code, as

displayed in Figure 3.7(a). The gradual change of the absorption depths with water vapor concentration may be understood from the figure and may be compared with the inset of Figure 3.2. The change occurs more predominantly with CO_2-1 band.

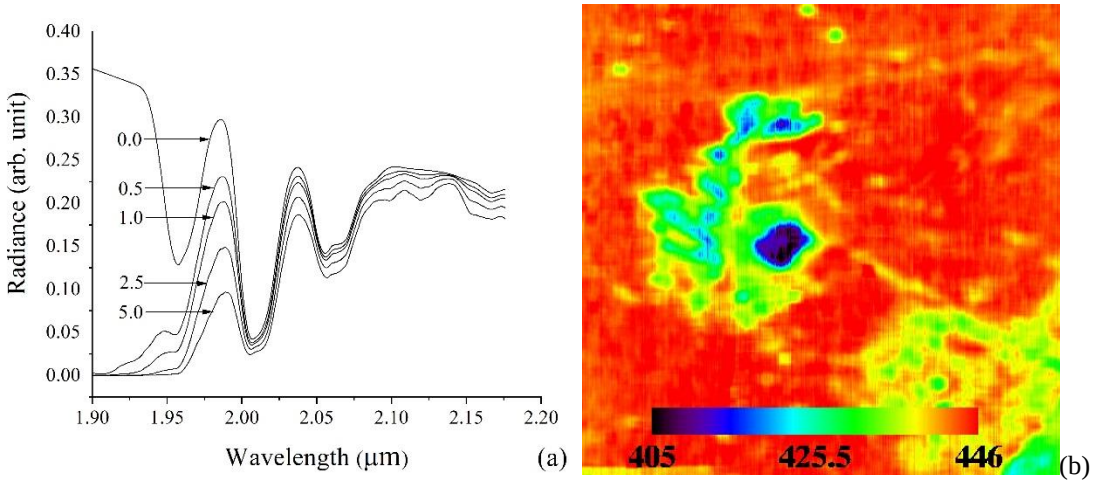

Figure 3. 7. (a) MODTRAN6 simulations of CO_2 absorption bands for tropical urban atmosphere with different water vapor concentrations (g cm^{-2}) indicated against the curves. Atmospheric profile: tropical urban, assumed CO_2 concentration 400 ppm, surface reflectance 10%, Lambertian and sensor altitude 6 km. (b) Spatial distribution of CO_2 concentration (ppm) estimated from CO_2-1 absorption band for the AVIRIS-NG image of Figure 3.6(a) using the same *a*-DOAS algorithm of section 3.1.3 and including 9% increase for water vapor effect on the absorption depth.

The correction procedure is as follows. A number of spectral curves similar to Figure 3.7(a) were generated with MODTRAN6 and the radiance ratio (L_0/L) for CO_2-1 band was determined for each case. During the image procurement, the water vapor concentration was around 2.8 g cm^{-2}. For such a value, the CO_2 concentration was found to be increased by about 9% with respect to the assumed value for simulation. Therefore, an enhancement of the same 9% was considered in estimating the CO_2 concentration from CO_2-1 band.

Figure 3.7(b) shows the spatial distribution of CO_2 concentration (ppm) estimated from CO_2-1 absorption band for the same AVIRIS-NG image of Figure 3.6(a) using the same and including 9% increment for the water vapor correction mentioned above. The results are in close agreement with those obtained with CO_2-2 band [Figure 3.6(b)].

Figures 3.5 and 3.6 present a single example of imaging spectroscopy. The same technique was implemented to the images of the whole region around 22° 33′ 30″ N, 88° 17′ 30″ E and 22° 32′ 30″ N, 88° 19′ 30″ E and the spatial variation of CO_2 concentration was found to be from 291 to 445 ppm for CO_2-1 band and from 350 to 466 ppm for CO_2-2 band. Such capability of the present method to distinguish slight local variations in CO_2 concentration is expected to detect natural or man-made point sources of CO_2 emission over small area, as will be discussed in Chapter 4.

The conventional technique (Spinetti et al., 2008) of comparing with radiative transfer simulation was also executed with the present images and was compared with the present results. The continuum Interpolated Band Ratio (CIBR) can be expressed as an inverse of Eq. (3.2) and the CIBR is expressed as $\exp[-\alpha®^{\beta}]$ where α and β are two parameters representing the model variables (Spinetti et al., 2008). Many radiance spectral curves were simulated with MODTRAN6 for different values of CO_2 ppm and the values of α and β were determined by fitting with the assumed CO_2 values. Putting the values of α and β determined this way to the image-derived CIBR, the CO_2 concentrations were estimated for all image pixels. The results are displayed in figures 3.7(a) and 3.7(b), respectively. These results also discriminate the CO_2 concentrations at vegetated and non-vegetated regions. However, comparing with the present results of figures 3.5(b) and 3.6(b), it is understood that the conventional technique gives rise to large difference between the CO_2 concentrations from the two absorption bands. Moreover, an underestimated value is obtained from CO_2-2 band. The present technique, of course, yields more consistent results.

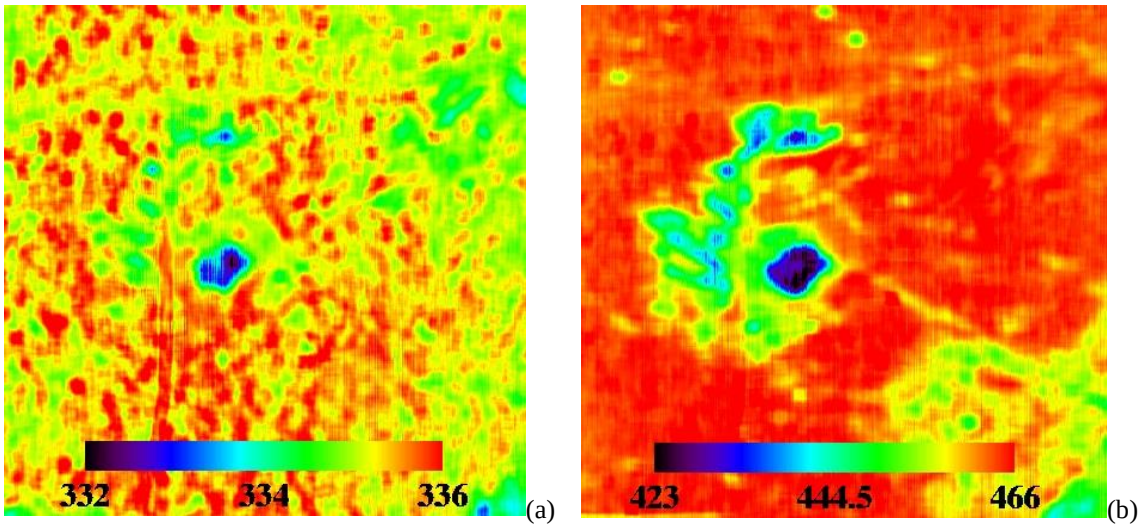

(a) (b)

Figure 3. 8. Spatial spreading of CO_2 concentration (ppm) assessed from (a) CO_2-2 and (b) CO_2-1 absorption band for the AVIRIS-NG image segment of Figure 3.6(a) by the conventional image-derived CIBR technique using MODTRAN6 simulated model parameters.

3.5. Water Vapour (H_2O) Correction using Martian Spectra

This section presents another novel technique for implementing H_2O correction to CO_2 absorption and proper recovery of the depth and shape of the CO_2 absorption profile. The method is based on the comparison of the terrestrial atmospheric radiance spectra with the atmospheric radiance spectra of planet Mars where CO_2 is the major atmospheric component at very low atmospheric pressure and the presence of H_2O in the atmosphere is negligible (Read et al., 2015; Montmessin and Ferron, 2019). Assuming the spectral signature of CO_2 in the Martian atmosphere as a model, the present work compares the radiance spectra derived from AVIRIS-NG images with that obtained from the Compact Reconnaissance Imaging Spectrometer (CRISM) hyperspectral images for Mars and also with MODTRAN-simulated synthetic spectra to propound that the truncation of CO_2 absorption depth caused by H_2O absorption can be rectified through a proportionality constant representing the ratio of the two consecutive CO_2 bands. This method is easy and is likely to enhance the usefulness of the shortwave infrared channels of the medium

resolution, general purpose imaging spectrometers (Griffin et al., 2005; Guanter et al., 2015; Chapman et al., 2019) in connection with the estimate of atmospheric CO_2.

3.5.1. Data Sources

This work involves two different types of atmospheric spectra, one of the earths and the other of Mars. These are derived from two different imaging systems of comparable spectral resolution. The earth radiance spectra derived from AVIRIS-NG are already introduced. These cover the range of 0.3764 to 2.5001 μm with the resolution of 0.005 μm per channel. The images of Mars procured by CRISM having the range of 1.002 to 3.920 μm with the resolution of 0.00655 μm per channel were downloaded from open source (http://crism.jhuapl.edu/data/publicData.php). Sixteen Martian images of radiance record were taken avoiding the polar region, for the period of November 2016 to August 2017, thus spanning almost one earth-year. Fifty random spectra were taken from each image. The spectra were derived with CRISM Analysis Tool (CAT) v7.4 (https://pds-geosciences.wustl.edu/missions/mro/crism.htm) plugged into ENVI+IDL v5.3 image processing software.

The CO_2 absorption band at larger wavelengths around 4.3 μm in the Martian atmosphere is found to change with space and time (Montmessin et al., 2007). Though the range is beyond the present scope and no such discrepancy is reported for the absorption at the wavelengths of present interest, the large number of spectra were collected with the intention of minimizing the random error. For AVIRIS-NG images also, fifty random spectra were collected from each of three dominant features, namely vegetation, waterbody and densely populated urban regions.

3.5.2. Image-derived Spectra

Spectral subsets of 1.9 to 2.2 μm were sorted out from each type of Martian and terrestrial spectra mentioned above. Both included the CO_2 absorption information of own category. Then a representative spectrum of each category was generated by the singular value

decomposition (SVD) technique. The data matrix **A** incorporating the spectral data was decomposed into the following three components as

$$\mathbf{A} = \mathbf{USV}^{T} \tag{3.5}$$

Each column of **A** in Eq. (3.5) represents a separate spectrum of 47 wavebands collected on a different sample and each row of **A** denotes the radiance at a given wavelength for different samples. The first column of **U** or the first row of $\mathbf{V}^T$ represents the principal component and the diagonal elements of **S** are the singular values of **A**. In the present standardization for representative spectra, **A** is (47×48) matrix, **U** is (47×47) matrix and $\mathbf{V}^T$ is (48×48) matrix. The diagonal elements of **S** are (47×48). The first column of **U** was taken as the representative spectrum in each case.

3.5.3. Synthetic Spectra

The synthetic radiance spectra were simulated with MODTRAN6 (Spectral Sciences Inc.) code, which is a widely used commercial software for modelling the propagation of electromagnetic radiation through user-specified atmospheric states with high spectral resolution taking into account surface reflection, atmospheric transmission, absorption and scattering. All these functions are integrated in the form of a package containing many built-in surface, altitude and atmospheric models, such as rural, urban, desert, maritime etc. with the provision for user-defined options.

Simulations were carried out over a large range, 100 to 600 ppm of CO_2. The H_2O concentration was varied from zero up to 7.0 g cm^{-2}, which is feasible to India's tropical atmosphere (Rangarajan and Mani, 1982). Diversified surface features were included in the simulations. For aerosols, MODTRAN contains a function library for generating radiometric properties of climatology-based atmospheres and particulate having various user-defined functional forms for particle size distributions. Considering possible aerosol radiative effects (Lolli et al., 2019), the built-in aerosol models in the software for urban, rural and other atmospheric conditions were implemented in each case, as applicable.

3.5.4 Martian and Terrestrial Radiance Spectra

Figure 3.9 depicts the signatures of CO_2 absorption on the radiance spectra of Martian atmosphere derived from CRISM images in different seasons. Three consecutive CO_2 absorption bands about 2 μm, henceforth named as CO_2-1, CO_2-2 and CO_2-3, are visible on the spectral curves.

The radiance spectra for the earth's atmosphere derived from AVIRIS-NG images are already introduced and the CO_2 absorption bands are also highlighted (Figures 3.1 and 3.2). For convenience, similar spectral absorptions are shown in Figure 3.10 for three different features, namely vegetation, waterbody and urban regions. The SVD representation has fetched the same scale for the diversified surface reflectivity of different objects. Comparing figures 3.8 and 3.9, it is noted that the leftmost band (CO_2-3) present in the Martian atmosphere gets completely masked by H_2O absorption in the earth's atmosphere and is not of present attention. The rightmost band (CO_2-2) is almost free from H_2O absorption. The middle-band (CO_2-1) is partly overlapped by H_2O absorption but it is the most prominent absorption band out of these three.

The trends of change of CO_2 and H_2O absorptions in earth's atmosphere are explained in detail using the MODTRAN simulated radiance spectra of Figure 3.11. It demonstrates that on decreasing the H_2O concentration from 7.0 g cm^{-2} up to zero [Figure 3.9(a)], the earth-like spectral shape, similar to that of Figure 3.10 gradually changes and assumes a shape like that of Mars, similar to that of Figure 3.9. The CO_2-3 band hidden under the H_2O absorption gets revealed and the middle CO_2-1 band acquires its actual depth. Such observations also indicate that out of these three absorption bands, CO_2-1 is the most sensitive one to the concentration of CO_2 and the correction for H_2O absorption applied to this band may produce the most appropriate value of CO_2.

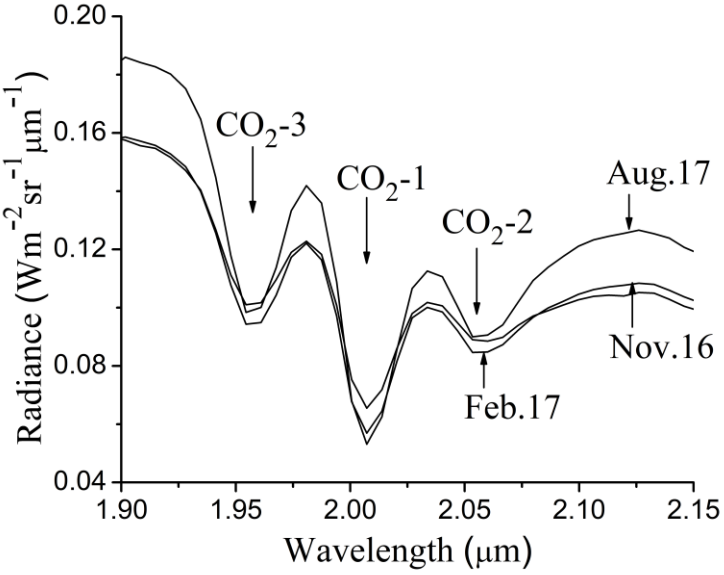

Figure 3. 9. Radiance spectra for Mars derived from CRISM images at different seasons indicated against the curves. Three CO_2 absorption bands designated as CO_2-1, CO_2-2 and CO_2-3, respectively are visible on the radiance spectral curves.

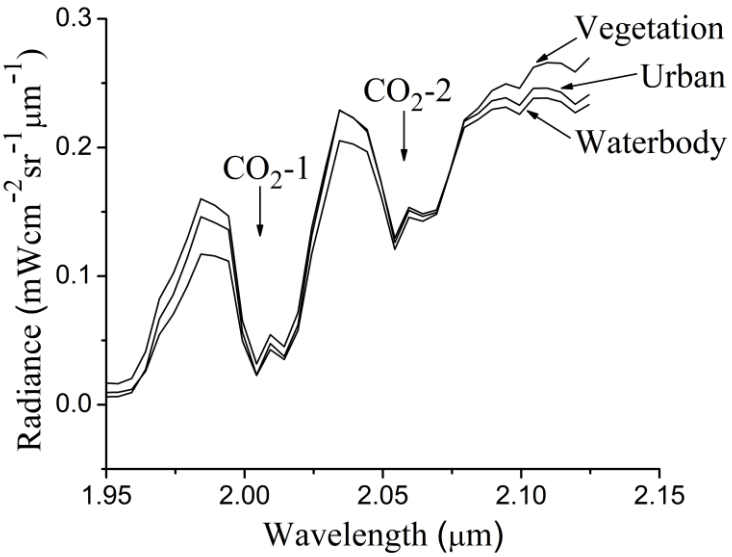

Figure 3. 10. Terrestrial atmospheric radiance spectra derived from AVIRIS-NG images for vegetation, waterbody and urban regions. The CO_2-1 and CO_2-2 absorption bands are visible.

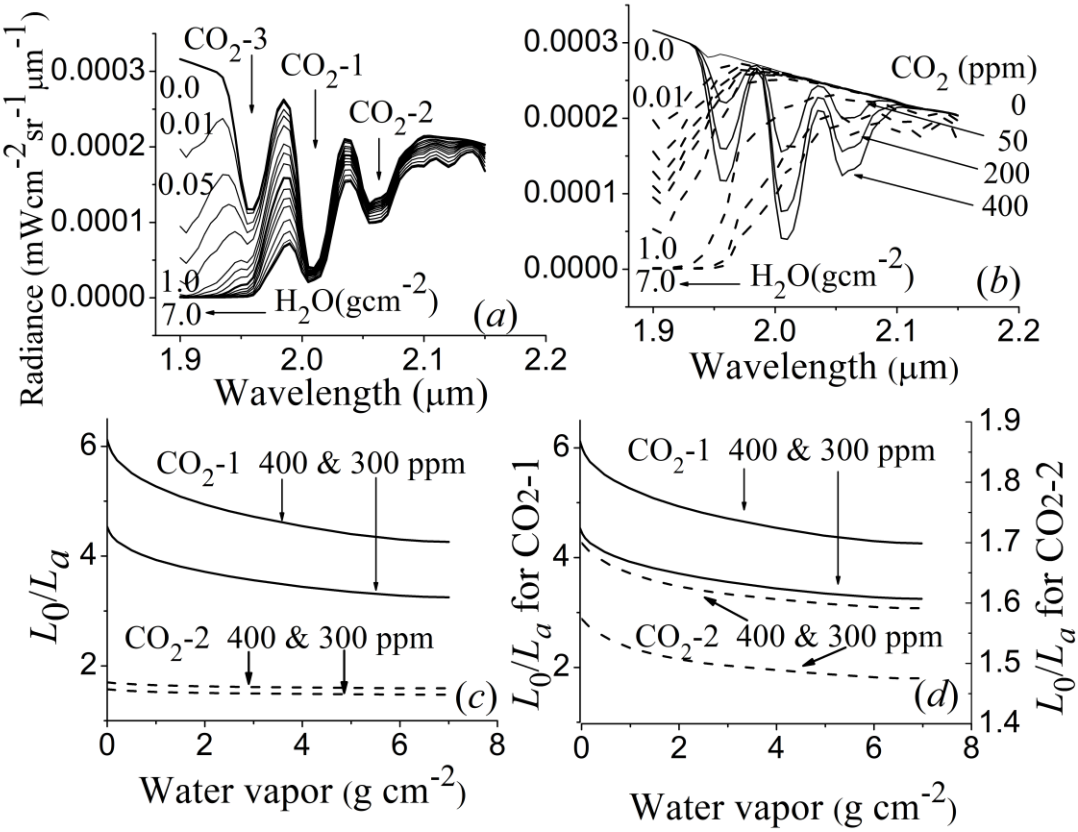

Figure 3. 11. MODTRAN simulated radiance spectra illustrating: (a) absorption due to different H_2O concentrations (gcm^{-2}) with 400 ppm of CO_2 concentration, (b) overlapping of CO_2 absorption with zero H_2O (solid lines) and H_2O absorption with zero CO_2 (dashed lines), radiance ratio (L_0/L_a) of CO_2-1 and CO_2-2: (c) in the same scale and (d) in individual scales.

Figure 3.11(b) indicates that the H_2O absorption modifies both CO_2-1 and CO_2-2 depths but CO_2-2 is much less affected. This is made more prominent with their individual radiance ratios (L_0/L_a) in the same scale [Figure 3.11(c)]. However, Figure 3.11(d) affirms that the trends of variation with H_2O concentration is the same for both the absorptions and consequently their ratio would vary proportionally for finite CO_2 concentrations. For a certain CO_2 concentration, both the CO_2-1 and CO_2-2 absorption depths undergo similar trend of variation with water vapor concentration so that their ratio varies almost linearly, at least for practical purpose.

3.5.5. Correction Parameter ®

The above findings on terrestrial, Martian and synthetic spectra put up the concept that the actual absorption depth of CO_2-1 band in absence of H_2O and its truncation in presence of H_2O can be correlated in terms of the ratio ® of the more affected (CO_2-1) and the less affected (CO_2-2) absorption depths. Consequently, the original CO_2-1 depth can be retrieved from the experimentally obtained truncated depth in terms of R. The physical significance is that the value of R for a certain combination of CO_2 (unknown) and H_2O (known) concentration acts as a proportionality constant that can predict the extent of compensation for the truncation of CO_2-1 absorption band.

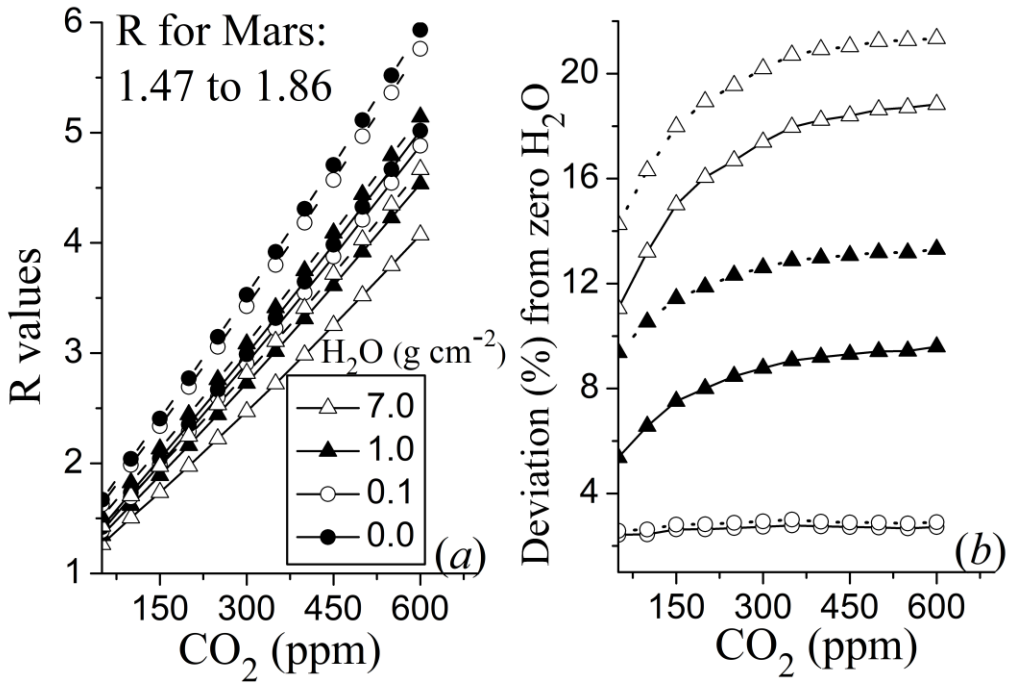

Figure 3. 12. (a) Variation of CO_2-1 to CO_2-2 absorption depth ratio ® with CO_2 (ppm) and H_2O (g cm^{-2}) concentrations simulated with MOdTRAN6 for tropical atmosphere of the earth with two different surface features: urban (solid line) and grassland (dashed line). (b) The corresponding percentage deviation in R from that with zero water vapor (symbols are same as those of Figure 3.12(a).

Figure 3.12(a) explains the above phenomena with simulated variation of R determined from synthetic spectra over large ranges of CO_2 and H_2O concentrations with

two different surface features. It is encouraging to note that the *R* values for the Martian spectra (mentioned in the figure) are also of the same order. The CO_2 column of Mars has much larger vertical mass (≈150 kg m^{-2}) than that of terrestrial CO_2 (≈4 kg m^{-2}). Also, the two atmospheres are totally different. In spite of such large differences in the atmospheric conditions, the R values for the Martian spectra are 1.47 to 1.86 whereas that of the earth is 1 to 6 for wide variation of H_2O. Getting such comparable values of *R* is obviously a strong experimental support to consider this radiation absorbing property of CO_2 molecules as a universal phenomenon. Figure 3.12(a) suggests that the extent of reduction of CO_2-1 absorption band for a specific H_2O concentration can be compensated for simply by the proportionality constant ® predicted from theoretical calculations. Figure 3.12(b) presents some examples of percentage change in *R* from that of zero H_2O state for varying CO_2 and H_2O concentrations and concludes that whatever CO_2-1 depth is obtained from the terrestrial spectra in presence of H_2O, can be multiplied by a constant term to obtain the corrected value.

Table 3. 4. Comparison of *R*-values for synthetic (MODTRAN simulated) and AVIRIS-NG spectra.

Synthetic Spectra with and without H_2O absorption			AVIRIS-NG Spectra	
Surface (aerosol)	R without H_2O	R with H_2O (*% decrease*)	Surface	R
Desert (desert)	3.32	2.87 (*13.55*)	--	--
Grassland (rural)	3.66	3.10 (*15.30*)	Vegetation	2.67
Urban (urban)	3.24	2.78 (*14.19*)	Urban	3.01
Wetland (rural)	3.12	2.70 (*13.46*)	Waterbody	2.71
Parameters: tropical atmosphere, CO_2 = 400 ppm, H_2O = 0 or 2.8 g cm^{-2}				

Table 3.4 validates the above process through comparison of *R*-values obtained with MODTRAN6 simulated synthetic spectra and the actual spectra derived from AVIRIS-NG images for different surface features. For the synthetic spectra, R values are estimated with and without H_2O absorption. The corresponding aerosol models are mentioned within brackets. The assumed H_2O concentration of 2.8 g cm^{-2} for the

simulation is close to that existing while image procurement and field measurement. Comparing the results obtained on the synthetic spectra with and without H_2O absorption imply that the H_2O absorption diminishes the R value by ≈ 13–15%, almost up to the same extent irrespective of the surface and atmospheric conditions. The AVIRIS-NG spectra, which is naturally affected by the H_2O absorption, produce comparable R values for similar surface features. An average increase of 14% in the CO_2-1 absorption depth is implemented in the present case of CO_2 assessment from AVIRIS-NG images.

3.5.6. Spatial CO_2 Distribution with H_2O Correction

Some results on this H_2O correction technique are depicted in Figure 3.13. It compares some samples of spatial distribution of CO_2 (ppm) estimated from AVIRIS-NG images with and without H_2O correction. The CO_2 concentrations derived from both CO_2-1 and CO_2-2 bands are included, as mentioned in the figure caption.

Two image segments, namely (A) and (B) are taken from densely populated urban area. The difference is that image (A) contains a large and distinct vegetated area. It is actually a big botanical garden and human activities are negligible within this area. The corresponding CO_2 maps [(C) and ®] indicate reduced amount of CO_2 in this region. Image (B) has no such distinction of vegetated region, which is reflected in the uniform CO_2 distributions of (D) and (F).

It is understood from the above images that the absorption of CO_2-1 can discriminate the spatial CO_2 variation more distinctly than obtained with CO_2-2. However, the mean CO_2 value obtained from CO_2-1 absorption is much lower than that CO_2-2. Then the correction for H_2O absorption is implemented to CO_2-1 absorption and the results are shown in images (G) and (H). Now the average CO_2 level rises up and becomes closer to that obtained from CO_2-2 absorption. Now both the CO_2 absorption bands yield consistent results. The present correction of 14% increase is situation-specific. It is changeable with the climatic condition and the H_2O concentration at the time of image procuring. However, the methodology is generalized and a similar technique can be

adopted with proper input parameters for determining the correction term for other images.

The column average value of CO_2 estimated by conventional DOAS technique from the concurrent ground spectroradiometric measurements ranged from 336 to 438 ppm, of the same order of that obtained from AVIRIS-NG in Figure 3.13 after the correction. A good consistency was thus obtained with ground-based and airborne measurements. The surface-level CO_2 was, however, much higher. It varied from 386 to 542 ppm for places of different urban congestions. This topic is discussed in Chapter 6.

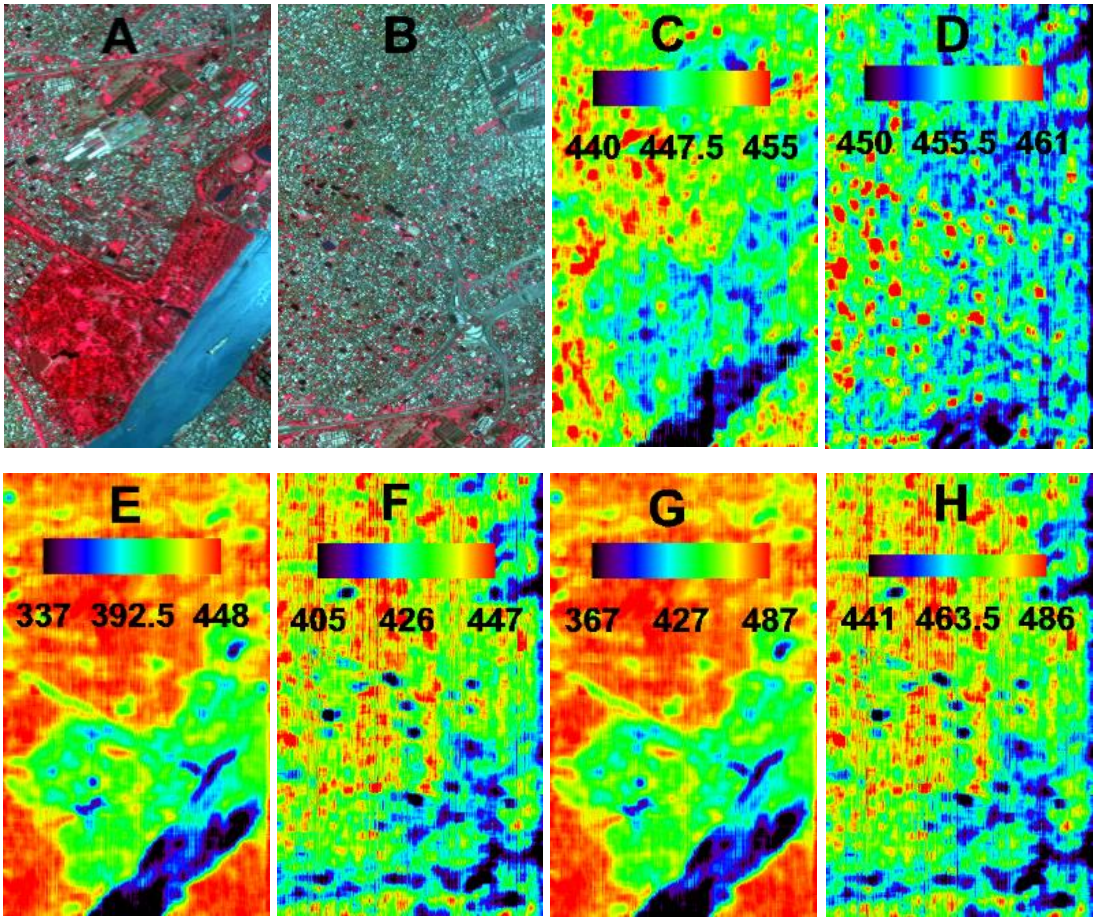

Figure 3. 13. (A) and (B) are AVIRIS-NG image segments of densely populated areas. The corresponding CO_2 concentration (ppm) distributions are derived in (C) and (D), respectively using CO_2-2 absorption depth. The CO_2 distributions for the same two regions retrieved from CO_2-1 absorption depth are given in ® and (F), respectively. The distributions retrieved from CO_2-1 with H_2O correction are given in (G) and (H), respectively.

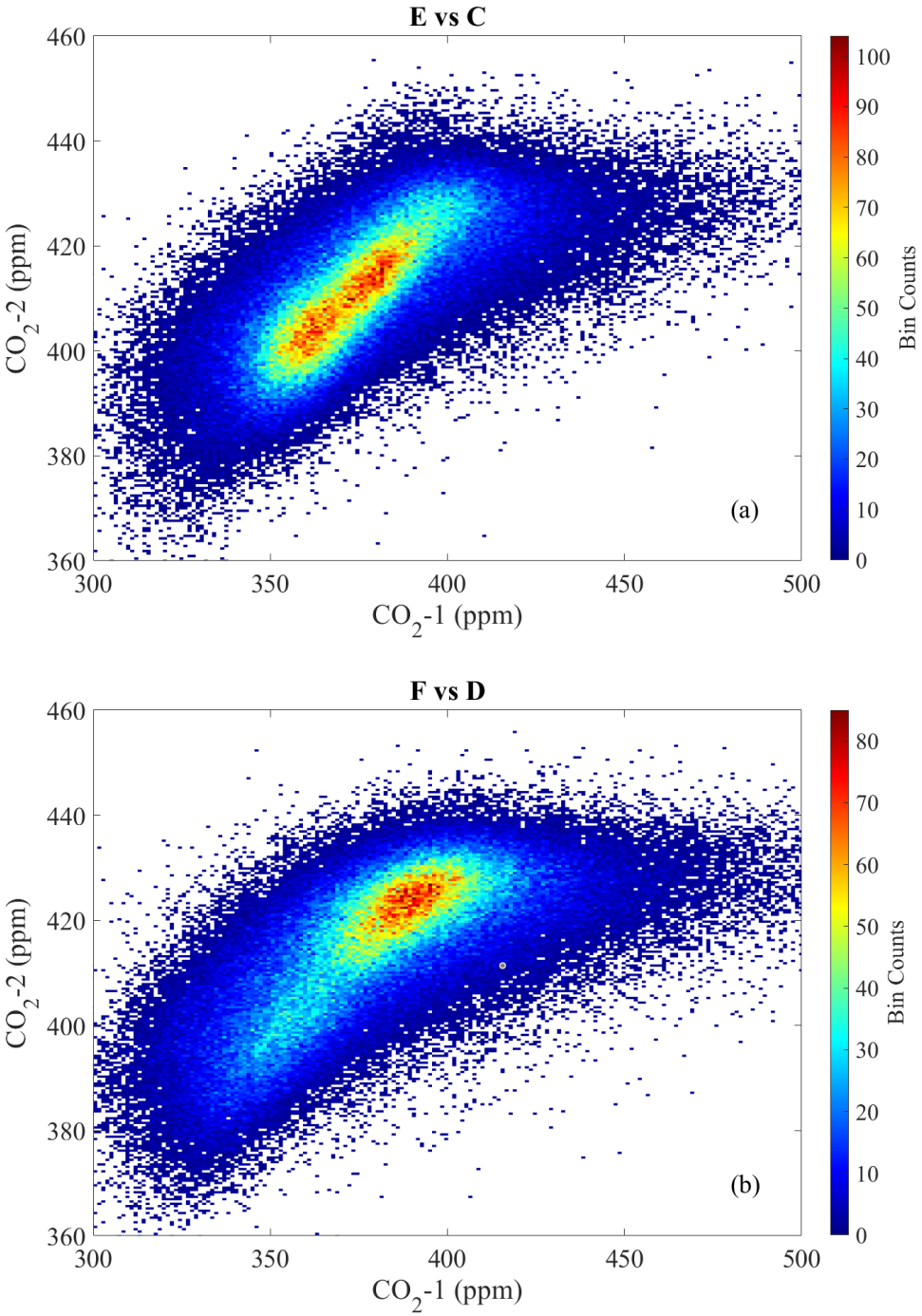

Figure 3. 14. Binned scatter plot of CO_2 values estimated from CO_2-1 and CO_2-2 band of (a) Figure 3.13® vs (C) and (b) Figure 3.13(F) vs (D).

Figure 3.14(a) describes the density of pixels for different CO_2 concentrations estimated from CO_2-1 and CO_2-2 band for the image depicted in Figure 3.13® and (C) referred to the Figure 3.13(A) image segment. Figure 3.14(b) is the same for Figure 3.13(F) and (D) referred to Figure 3.13(B). It must be noted that in Figure 3.14(a) some broadening or splitting of the denser region in red can be seen whereas in Figure 3.14(b) there is one bright red spot. This splitting can be explained by the existence of two different CO_2 concentrations spread out in the major areas of Figure 3.13(A) which is evidently contains urban regions with a wide area of vegetation. Whereas there are no major vegetated regions in Figure 3.13(B) explaining the high CO_2 level spot (Figure 3.14(b)) for maximum of the pixels. An overall lower CO_2 value can also be observed for both CO_2-1 and CO_2-2 in Figure 3.14(a) which contains vegetation than Figure 3.14(b) which is mainly of urban areas.

3.6. Inferences

This work combines ground based spectroradiometry and airborne image analysis and proposes a new technique for radiation absorption spectroscopy, termed as a-DOAS for the assessment of atmospheric trace gas. The method is based on averaging the absorption depths in terms of linear sum of radiance at the absorbing and non-absorbing wavelengths assigned with proper weights. The proposed technique has been validated with the retrieval of atmospheric CO_2 concentration from AVIRIS-NG images procured from urban areas of India for the first time. It has been able to estimate the spatial variation of CO_2 and to distinguish the CO_2 concentrations of vegetated and non-vegetated regions. It thus highlights the potential of the technique to detect local changes in CO_2 concentration from high spatial resolution images. This topic is studied further in Chapter 4.

In a tropical country like India, water vapour is a significant agent of the atmosphere and one should account for the water vapor absorption band adjacent to 2 μm while calculating the CO_2 absorption depth (Figure 3.2). This work has developed two different techniques for such H_2O correction. The first one is based on the fitting of simulated radiance ratio (L_0/L) for CO_2-1 band for different CO_2 concentration (ppm) with

water vapor concentration (g cm^{-2}). The second method, more oriented to experimental data, compares the radiance spectra of the earth's atmosphere with that of Martian atmosphere where CO_2 is the main ingredient and H_2O is negligible. The radiance spectra of Mars' ®e were used as a model. The gradual change of the radiance spectra from 'earth-like' to 'Mars-like' and the corresponding changes of the CO_2 absorption depths are explained with MODTRAN6 atmospheric simulator for different surface and atmospheric conditions. The technique suggests that the actual CO_2-1 absorption depth in absence of H_2O and its reduction in presence of H_2O can be interrelated in terms of the ratio ® of the more affected (CO_2-1) and the less affected (CO_2-2) absorption depths and the original CO_2-1 depth can be retrieved from the experimentally obtained truncated depth in terms of R. The findings are validated with AVIRIS-NG images.

Chapter References

Chapman, J. W., Thompson, D. R., Helmlinger, M. C., Bue, B. D., Green, R. O. & Eastwood, M. L. et al. (2019). Spectral and Radiometric Calibration of the Next Generation Airborne Visible Infrared Spectrometer (AVIRIS-NG). *Remote Sensing*, 11(18), 2129. Doi: 10.3390/rs11182129

Griffin, M., Hsu, S., Burke, H., Orloff, S., & Upham, C. (2005). Examples of EO-1 Hyperion Data Analysis. *LINCOLN LABORATORY JOURNAL*, 15(2), 271-298.

Guanter, L., Kaufmann, H., Segl, K., Foerster, S., Rogass, C. & Chabrillat, S. et al. (2015). The EnMAP Spaceborne Imaging Spectroscopy Mission for Earth Observation. *Remote Sensing*, 7(7), 8830-8857. Doi: 10.3390/rs70708830

Lolli, S., Khor, W. Y., Matjafri, M. Z. & Lim, H. S. (2019). Monsoon Season Quantitative Assessment of Biomass Burning Clear-Sky Aerosol Radiative Effect at Surface by Ground-Based Lidar Observations in Pulau Pinang, Malaysia in 2014. *Remote Sensing*, 11(22), 2660. Doi: 10.3390/rs11222660

Montmessin, F., Gondet, B., Bibring, J., Langevin, Y., Drossart, P. & Forget, F. et al. (2007). Hyperspectral imaging of convective CO_2 ice clouds in the equatorial mesosphere of Mars. *Journal of Geophysical Research*, 112(E11), doi: 10.1029/2007je002944

Rangarajan, S., & Mani, A. (1982). Total precipitable water in the atmosphere over India. *Proc. Indian Acad. Sci. (Earth Planet. Sci.)*, 91(3), 189-207.

Raychaudhuri, B., Chaurasia, S. & Roy, S. (2019). Spatial variation of atmospheric carbon dioxide concentration retrieved from AVIRIS-NG images including water vapor correction and spectroradiometric validation for two urban places of India. *Remote Sensing of Clouds and the Atmosphere XXIV*, doi: 10.1117/12.2532027